High Frame Rate Imaging System for Limited Diffraction Array Beam Imaging with Square-Wave Aperture Weightings

Jian-yu Lu, *Senior Member, IEEE*, Jiqi Cheng, and Jing Wang

Abstract—A general-purpose high frame rate (HFR) medical imaging system has been developed. This system has 128 independent linear transmitters, each of which is capable of producing an arbitrary broadband (about 0.05–10 MHz) waveform of up to ±144 V peak voltage on a 75-ohm resistive load using a 12-bit/40-MHz digital-to-analog converter. The system also has 128 independent, broadband (about 0.25–10 MHz), and time-variable-gain receiver channels, each of which has a 12-bit/40-MHz analog-to-digital converter and up to 512 MB of memory. The system is controlled by a personal computer (PC), and radio frequency echo data of each channel are transferred to the same PC via a standard USB 2.0 port for image reconstructions.

Using the HFR imaging system, we have developed a new limited-diffraction array beam imaging method with square-wave aperture voltage weightings. With this method, in principle, only one or two transmitters are required to excite a fully populated two-dimensional (2-D) array transducer to achieve an equivalent dynamic focusing in both transmission and reception to reconstruct a high-quality three-dimensional image without the need of the time delays of traditional beam focusing and steering, potentially simplifying the transmitter subsystem of an imager. To validate the method, for simplicity, 2-D imaging experiments were performed using the system. In the *in vitro* experiment, a custom-made, 128-element, 0.32-mm pitch, 3.5-MHz center frequency linear array transducer with about 50% fractional bandwidth was used to reconstruct images of an ATS 539 tissue-mimicking phantom at an axial distance of 130 mm with a field of view of more than 90°. In the *in vivo* experiment of a human heart, images with a field of view of more than 90° at 120-mm axial distance were obtained with a 128-element, 2.5-MHz center frequency, 0.15-mm pitch Acuson V2 phased array. To ensure that the system was operated under the limits set by the U.S. Food and Drug Administration, the mechanical index, thermal index, and acoustic output were measured. Results show that higher-quality images can be reconstructed with the square-wave aperture weighting method due to an increased penetration depth as compared to the exact weighting method developed previously, and a frame rate of 486 per second was achieved at a pulse repetition frequency of about 5348 Hz for the human heart.

I. Introduction

O NE of the limited-diffraction beams, the Bessel beam, was first studied theoretically by Stratton [1] and then experimentally by Durnin *et al.* [2]–[3]. In 1991, new families of limited-diffraction beams such as X waves were discovered [4]–[8]. X waves are multiple-frequency waves that have the same phase and group velocity. Theoretically, limited-diffraction beams can propagate to an infinite distance without spreading. In practice, when these beams are produced with finite aperture and energy, they have a large depth of field. Because of this property, limited-diffraction beams have potential applications in medical imaging [9]–[11], tissue identification [12], nondestructive evaluation of materials [13], Doppler blood flow measurement [14]–[15], fast computation of fields of two-dimensional (2-D) array transducers [16], optical communications [17], and other optics- [18] and physics-related areas [19]. Recently, X waves have been studied in nonlinear optics [20] and reported in the "Search and Discovery" column of [21].

Based on the studies of limited-diffraction beams [22]–[23], a 2-D and three-dimensional (3-D) high frame rate (HFR) imaging method was developed in 1997 [24]–[26], with its importance reported in [27], allowing both fast anatomical and blood flow velocity vector field imaging [28]. Recently, the method was extended [29]–[31] to include explicitly previous methods that used multiple transmissions with limited-diffraction array beams [14], [24]–[26], [32] and steered plane waves (see the Introduction and Item J of the Discussion of [24], and the Introduction, Item B.4. of the Discussion, and Fig. 8 of [25]) [33]–[35]. The extended HFR imaging method increases image resolution and field of view [36] and reduces sidelobes [29]–[31] as compared to the conventional delay-and-sum (D&S) methods with a fixed transmission focus and dynamically focused reception [37]. As more and more limited-diffraction array beams of different parameters or plane waves steered at different angles are transmitted (lower image frame rate), the image quality increases. The trade-off between the image quality and frame rate is useful for imaging of organs that do not move fast, such as the liver and kidney [29]–[31].

To experimentally study and further understand the imaging methods above, a general-purpose HFR imaging system was designed and constructed, and the details of its development are reported in this paper (see Section III-A) [38], [39].

Using the HFR imaging system and based on the extended HFR imaging method [29]–[31], we have developed a new limited-diffraction array beam imaging method with square-wave aperture voltage weightings. In this method,

two transmitters that have the same output amplitude but of an opposite sign are used to excite transducer elements to produce limited-diffraction array beams with two levels of quantization. In each transmission, one of the two transmitters is selected for each transducer element through a switch according to the sign of the sine and cosine functions (limited-diffraction array beam weighting functions) at the location of the element. The method can also be implemented with a single transmitter to reduce further the number of transmitters. However, this may reduce the transmission power and increase the image reconstruction complexity. The method has several advantages. First, it reduces the number of transmitters needed and thus may simplify the transmitter subsystem of an imaging system, especially for systems that use transducers of a large number of elements such as a 2-D array. This is the case when compared to both the conventional D&S method [37], where one transmitter is usually required for each transducer element due to the delay of transmission signal for beam focusing or steering, and the extended HFR imaging method [29]–[31], where a large number of transmitters are used for exact limited-diffraction array beam aperture weightings. This is significant because modern transmitters are complicated and bulky due to the requirements that they must transmit broadband radio frequency (RF) arbitrary waveforms, work at a high output voltage, and have a large static current or power to improve linearity for applications such as nonlinear imaging [40] and coded excitations [41]. Second, because there is no amplitude tapering of voltage over the transducer aperture, the method increases transmission power and, thus, the signal-to-noise ratio (SNR) of the system. Third, according to the reciprocal principle, the square-wave aperture weightings can also be applied to reception (echo signals) to replace some high-speed digital signal processing in image reconstructions [42]. Finally, combined with the HFR image reconstruction algorithms that use the fast Fourier transform (FFT) [24]–[27], the method may help to develop high-quality 3D imaging systems that require fully addressable 2-D array transducers of a large number of independent elements.

To show the efficacy of the square-wave aperture weighting method, both *in vitro* and *in vivo* experiments were carried out with the HFR imaging system. For simplicity, 2-D, instead of 3-D, images were reconstructed. In the *in vitro* experiment, a custom-made, 128-element, 0.32-mm pitch, 3.5-MHz center frequency linear array transducer with about 50% fractional bandwidth was used to obtain images of an ATS 539 tissue-mimicking phantom (ATS Laboratory of Bridgeport, CT). In the *in vivo* experiment, an Acuson V2 phased array transducer (128 elements, 0.15-mm pitch, and 2.5-MHz center frequency; Siemens Medical Solutions USA, Inc., Malvern, PA) was used to obtain images of a human heart for an entire heart cycle (see the supplementary video 🎞️). Results show that the quality of images obtained with the square-wave aperture weighting method is higher than that with the exact limited-diffraction array beam weightings of the extended

HFR imaging [29]–[31] due to an increased SNR. The *in vivo* experiments indicate that the method also works well for fast moving organs such as the heart. As a comparison, results obtained with steered plane wave transmissions [29]–[31] and focused beam (focused at 70 mm) transmissions of the conventional D&S method with dynamic focusing in reception [37] are also shown.

To ensure safety in the *in vivo* experiments, the mechanical index (MI), thermal index (TI), and acoustic output (AO or $I_{\text{SPTA.3}}$, the attenuated spatial-peak, temporal-average intensity) of the system were measured for the two transducers used in the experiments [43]–[45] (see Table I). Results show that a higher pressure at the transducer surface may be allowed to increase the SNR for a plane-wave type of beams such as those produced with the square-wave aperture weightings than the traditional focused beams (see Section III-B for detail) without exceeding the upper limits (such as 1.9 for the MI) of the safety parameters [43].

This paper is organized as follows: In Section II, theoretical preliminaries of limited-diffraction array beam imaging with square-wave aperture voltage weightings are given. The theoretical derivations start from the X wave solutions to the wave equation, and thus they are more complete and easier to follow than previously reported [29]–[31], although the current presentation is more concise. In addition, the derivations generalize the relationship that the limited-diffraction array beam aperture weightings [24]–[26] of echo signals are identical to the 2-D spatial Fourier transform of the signals over the same transducer aperture [29]–[31] to an arbitrary transmission beam. In Section III, the general-purpose HFR imaging system is introduced and the measurement of the standard safety parameters (MI, TI, and AO) of the system is reported. *In vitro* experiments on a phantom, *in vivo* experiments on a human heart, and their results are shown in Section IV. Finally, a conclusion is given in Section V.

II. THEORETICAL PRELIMINARIES

To understand the method of limited-diffraction array beam imaging with square-wave aperture weightings, it is helpful to summarize briefly the extended HFR imaging method [29]–[31] and relate it to the X wave theory [4]–[8] for completeness. From the theory, it is shown that the relationship that the limited-diffraction array beam aperture weightings [24]–[26] on echo signals are identical to the 2-D Fourier transform of the signals on the same transducer aperture can be generalized to an arbitrary transmit beam. The theory also makes it clear that with the square-wave aperture weightings, the transmission scheme of an imager could be simplified from that of the traditional D&S method [37]; that is, in principle, only one or two transmitters are needed to implement a 3-D ultrasound imaging system. In addition, the square-wave aperture-weighting concept can also be extended to reception beam forming, potentially simplifying the high-speed digital circuits for image reconstructions [42].

TABLE I
MECHANICAL INDEX, THERMAL INDEX OF SOFT TISSUES, AND ACOUSTIC OUTPUT OF THE HFR IMAGING SYSTEM
FOR TWO DIFFERENT TRANSDUCERS.*

	Depth (mm)	Unfocused Beams (HFR)			Focused Beams (D&S)		
		MI	TI (TIS)	AO (mW/cm^2)	MI	TI (TIS)	AO (mW/cm^2)
V2	30	1.41	3.64	374.20	2.90	3.64	2770.77
2.5 MHz	40	1.47	3.64	427.56	2.54	3.64	2482.99
Transducer	60	1.16	3.64	412.32	1.68	3.64	1340.63
(19.2 mm)	70	0.99	3.64	299.38	1.32	3.64	843.84
	90	0.71	3.64	143.29	0.87	3.64	319.20
Custom	30	0.49	1.07	55.71	1.85	1.07	1166.97
3.5 MHz	40	0.46	1.07	52.89	1.64	1.07	1103.38
Transducer	60	0.36	1.07	38.91	1.11	1.07	530.28
(40.96 mm)	80	0.25	1.07	16.94	0.71	1.07	198.33
	100	0.16	1.07	7.44	0.45	1.07	88.76

* Abbreviations: mechanical index, MI; thermal index of soft tissues, TIS; acoustic output, AO or $I_{\text{SPTA.3}}$.
The column "Depth" means where the parameters were measured. For focused beams, the "Depth" is also
the focal length. For simplicity, the TIS was calculated by assuming a scanned mode with a scan length
larger than 1 cm (the maximum values of the TIS are thus independent of the depths listed), while AO was
obtained by assuming a non-scanned mode to show the highest values at the depths.

A. Generalization of High Frame Rate Imaging Theory

An N-dimensional isotropic/homogeneous wave equation is given by

$$\left[\sum_{j=1}^{N} \frac{\partial^2}{\partial x_j^2} - \frac{1}{c^2}\frac{\partial^2}{\partial t^2}\right]\Phi(\vec{r},t) = 0, \quad (1)$$

where x_j $(j = 1, 2, \ldots, N)$ represents rectangular coordinates in an N-dimensional space, $N \geq 1$ is an integer, $\Phi(\vec{r},t)$ is a scalar function (sound pressure, velocity potential, or Hertz potential in electromagnetics) of spatial variables, $\vec{r} = (x_1, x_2, \ldots x_N)$, and time t. The constant c is the speed of sound in a medium (or the speed of light in vacuum).

An X wave solution to (1) is given by (assuming $N = 3$, $x_1 = x$, $x_2 = y$, and $x_3 = z$) [4]–[8]:

$$\Phi_{X_n}(\vec{r}_0, t) = \Phi_{X_n}(r_0, \phi_0, z_0 - c_1 t)$$
$$= e^{in\phi_0}\int_0^\infty B(k)J_n(kr_0\sin\zeta_T)e^{-k[a_0 - i\cos\zeta_T(z_0 - c_1 t)]}dk,$$
$$(n = 0, 1, 2, \ldots), \quad (2)$$

where the subscript "X_n" represents an nth-order X wave, n is an integer, $\vec{r}_0 = (x_0, y_0, z_0) = (r_0, \phi_0, z_0)$ is a spatial point in the rectangular or cylindrical coordinates ($x_0 = r_0\cos\phi_0$ and $y_0 = r_0\sin\phi_0$) (see Fig. 1), r_0 is the radial distance, ϕ_0 is the polar angle, z_0 is the axial distance, $c_1 = c/\cos\zeta_T$ is both the phase and the group velocity of the wave, $0 \leq \zeta_T < \pi/2$ is the Axicon angle [46]–[47] of X waves (see Fig. 1), $J_n(\cdot)$ is the nth-order Bessel function of the first kind, $B(k)$ is any well-behaved function that can represent the transfer function of a practical acoustic transducer (or electromagnetic antenna), a_0 is a constant that determines the fall-off speed of the high-frequency

components of X waves, and $k = \omega/c$ is the wave number, where $\omega = 2\pi f$ is the angular frequency, and f is the temporal frequency. In the following, we assume that $\vec{r}_1 = (x_1, y_1, 0)$ is a point at the surface of the transducer (Fig. 1).

Summing the X waves in (2) over the index, n, with the weight, $i^n e^{-in\theta_T}$, broadband limited-diffraction array beams [14], [32] or pulsed steered plane waves (a plane wave is a special case of limited-diffraction beams) are obtained, which are also limited-diffraction solutions to (1) (see Eq. (3) of [24]):

$$\Phi_{\text{Array}}^T(\vec{r}_0, t)\sum_{n=-\infty}^{\infty}i^n e^{-in\theta_T}\Phi_{X_n}(r_0, \phi_0, z_0 - c_1 t)$$
$$= \int_0^\infty B(k)\left[\sum_{n=-\infty}^{\infty}i^n J_n(kr_0\sin\zeta_T)e^{in(\phi_0 - \theta_T)}\right]$$
$$\cdot e^{-k[a_0 - i\cos\zeta_T(z_0 - c_1 t)]}dk, \quad (3)$$

where $0 \leq \theta_T < 2\pi$ is a free parameter representing an azimuthal angle (see Fig. 1), the superscript "T" in $\Phi_{\text{Array}}^T(\vec{r}_0, t)$ means "transmission," and the subscript "Array" represents "array beams." Because of the following equality [48],

$$\sum_{n=-\infty}^{\infty}i^n J_n(kr_0\sin\zeta_T)e^{in(\phi_0 - \theta_T)} = e^{i(kr_0\sin\zeta_T)\cos(\phi_0 - \theta_T)}, \quad (4)$$

and (5) (see equation next page, and Fig. 1 for coordinate system), where k_{x_T} and k_{y_T} are projections of the transmission wave vector along the x_1 and y_1 axes, respectively, the array beams can be written as the Fourier transform pair in (6) (see next page) in terms of time (see Eqs. (5) and (6) of [24]), where $A(k) = 2\pi B(k)e^{-ka_0}$ is a transmitting transfer function of the transducer elements that includes both the electrical response of the driving

$$\begin{cases} k_{x_T} = k \sin \zeta_T \cos \theta_T = k_{1_T} \cos \theta_T \\ k_{y_T} = k \sin \zeta_T \sin \theta_T = k_{1_T} \sin \theta_T \\ k_{z_T} = k \cos \zeta_T = \sqrt{k^2 - k_{1_T}^2} \geq 0; \text{ where } k_{1_T} = \sqrt{k_{x_T}^2 + k_{y_T}^2} = k \sin \zeta_T \end{cases}, \tag{5}$$

$$\begin{cases} \Phi_{\text{Array}}^T (\vec{r}_0, t) = \dfrac{1}{2\pi} \displaystyle\int\limits_{-\infty}^{\infty} A(k)H(k)e^{ik_{x_T}x_0 + ik_{y_T}y_0 + ik_{z_T}z_0}e^{-i\omega t}dk \\ \widetilde{\Phi}_{\text{Array}}^T (\vec{r}_0, \omega) = \dfrac{A(k)H(k)}{c}e^{ik_{x_T}x_0 + ik_{y_T}y_0 + ik_{z_T}z_0} \end{cases}, \tag{6}$$
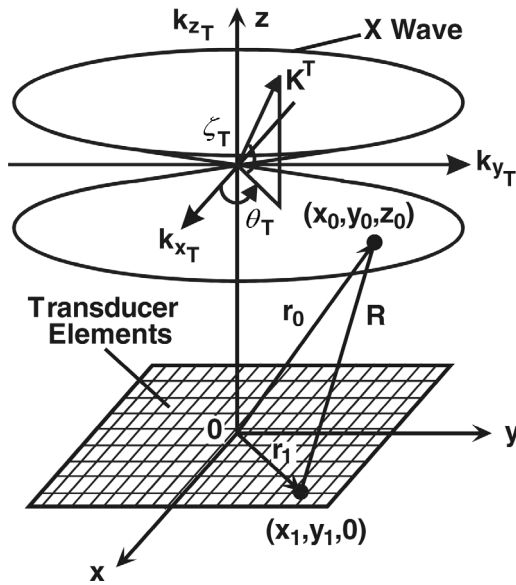

Fig. 1. Coordinates of transducer, Fourier space, and an X wave in space.

$\widetilde{\Phi}_{\text{Array}}^R (\vec{r}_0, \omega)$ is an expression of a monochromatic plane wave response steered at the direction along the reception wave vector; $\vec{K}^R = (k_x, k_y, k_z)$, where k_x and k_y are projections of the reception wave vector along the x_1 and y_1 axes, respectively; and $k_z = \sqrt{k^2 - k_x^2 - k_y^2} \geq 0$.

If the same array transducer is used as both transmitter and receiver, from (6) and (7), the received signal for the wave scattered from all point scatterers inside the volume, V, of an object function, $f(\vec{r}_0)$ (representing the scattering strength of a scatterer at point $\vec{r}_0$), is given by a linear superposition of individual scattering sources over V. This signal can be represented by the Fourier transform pair in (8) (see next page) in terms of time (see Eqs. (13) and (15) of [24]), where

$$\begin{cases} k_x' = k_x + k_{x_T} \\ k_y' = k_y + k_{y_T} \\ k_z' = k_z + k_{z_T} = \sqrt{k^2 - k_x^2 - k_y^2} + \sqrt{k^2 - k_{x_T}^2 - k_{y_T}^2} \geq 0 \end{cases}, \tag{9}$$

and "*" represents the convolution with respect to time. This uses the fact that the spectrum of the convolution of two functions is equal to the product of the spectra of the functions, and assumes that the imaging system is linear and multiple scattering can be ignored (first born or weak scattering approximation [51]–[52]). The 3-D spatial Fourier transform in (8) is defined the same as that in Eq. (14) of [24]. The relationship between the one-dimensional (1-D) temporal Fourier transform (spectrum) of the received echo signal that is weighted by a limited-diffraction array beam [14], [32], and the 3-D spatial Fourier transform of the object function is the key for image reconstructions (see Eqs. (16), (18), and (22) of [24]).

circuits and the electro-acoustical coupling characteristics [49], and $H(\omega/c) = \{1, \omega \geq 0; 0, \omega < 0\}$ is the Heaviside step function [50]. The spectrum of the array beam in (6) is an expression of a monochromatic (single angular frequency ω) plane wave steered at the direction along the transmission wave vector, $\vec{K}^T = (k_{x_T}, k_{y_T}, k_{z_T})$.

Similar to (6), the response of a transducer weighted with a broadband limited-diffraction array beam [14], [32] or pulsed steered plane wave for a point source (or scatterer) located at $\vec{r}_0$ is given by the following Fourier transform pair due to the reciprocal principle:

$$\begin{cases} \Phi_{\text{Array}}^R (\vec{r}_0, t) = \dfrac{1}{2\pi} \displaystyle\int\limits_{-\infty}^{\infty} T(k)H(k)e^{ik_x x_0 + ik_y y_0 + ik_z z_0}e^{-i\omega t}dk, \\ \widetilde{\Phi}_{\text{Array}}^R (\vec{r}_0, \omega) = \dfrac{T(k)H(k)}{c}e^{ik_x x_0 + ik_y y_0 + ik_z z_0} \end{cases}, \tag{7}$$

where the superscript "R" means "reception;" $T(k)$ is the transfer function of the transducer in reception;

B. Limited-Diffraction Array Beam Weighting and Spatial Fourier Transform of Echo Signals

Using (6) and (7), it is clear that (8) can be rewritten as (10) (see next page), where the last equal sign in (10)

$$
\begin{cases}
R_{k_x+k_{x_T}, k_y+k_{y_T}, k_z+k_{z_T}}(t) = \int_V f(\vec{r}_0) \left[\Phi_{\text{Array}}^T(\vec{r}_0, t)^* \, \Phi_{\text{Array}}^R(\vec{r}_0, t) \right] d\vec{r}_0 \\[2mm]
= \dfrac{1}{2\pi} \int\limits_{-\infty}^{\infty} \dfrac{A(k)T(k)H(k)}{c} \left[\int_V (\vec{r}_0) \, e^{i(k_x+k_{x_T})x_0 + i(k_y+k_{y_T})y_0 + i(k_z+k_{z_T})z_0} d\vec{r}_0 \right] e^{i\omega t} dk \\[2mm]
= \dfrac{1}{2\pi} \int\limits_{-\infty}^{\infty} \dfrac{A(k)T(k)H(k)}{c} F(k_x+k_{x_T}, k_y+k_{y_T}, k_z+k_{z_T}) \, e^{-i\omega t} dk \\[2mm]
\widetilde{R}_{k_x', k_y', k_z'}(\omega) = \dfrac{A(k)T(k)H(k)}{c} F(k_x', k_y', k_z')
\end{cases}
\tag{8}
$$

$$
\begin{aligned}
\widetilde{R}_{k_x', k_y', k_z'}(\omega) &= \int_V f(\vec{r}_0) \, \widetilde{\Phi}_{\text{Array}}^T(\vec{r}_0, \omega) \, \widetilde{\Phi}_{\text{Array}}^R(\vec{r}_0, \omega) \, d\vec{r}_0 \\[2mm]
&= \int_V f(\vec{r}_0) \, \widetilde{\Phi}_{\text{Array}}^T(\vec{r}_0, \omega) \, \Im_{x_1, y_1} \left\{ \Im_{k_x, k_y}^{-1} \left\{ \widetilde{\Phi}_{\text{Array}}^R(\vec{r}_0, \omega) \right\} \right\} d\vec{r}_0 \\[2mm]
&= \Im_{x_1, y_1} \left\{ \int_V \left[f(\vec{r}_0) \, \widetilde{\Phi}_{\text{Array}}^T(\vec{r}_0, \omega) \right] \left(-\dfrac{T(k)H(k)}{2\pi c} \dfrac{\partial}{\partial z_0} \left(\dfrac{e^{ik\sqrt{(x_1-x_0)^2+(y_1-y_0)^2+z_0^2}}}{\sqrt{(x_1-x_0)^2+(y_1-y_0)^2+z_0^2}} \right) \right) d\vec{r}_0 \right\}
\end{aligned}
\tag{10}
$$

is due to the shift theorem of Fourier transform and the following equality (see Eq. (13) of [53]):

$$
e^{ik_z z_0} = -\dfrac{1}{2\pi} \Im_{x_1, y_1} \left\{ \dfrac{\partial}{\partial z_0} \left(\dfrac{e^{ik\sqrt{x_1^2+y_1^2+z_0^2}}}{\sqrt{x_1^2+y_1^2+z_0^2}} \right) \right\},
\tag{11}
$$

where $\Im_{x_1, y_1}$ represents a 2-D Fourier transform in terms of both x_1 and y_1 at the transducer surface and $\Im_{k_x k_y}^{-1}$ is an inverse 2-D Fourier transform in terms of both k_x and k_y. Because the term,

$$
-\dfrac{1}{2\pi} \dfrac{\partial}{\partial z_0} \left(\dfrac{e^{ik\sqrt{(x_1-x_0)^2+(y_1-y_0)^2+z_0^2}}}{\sqrt{(x_1-x_0)^2+(y_1-y_0)^2+z_0^2}} \right),
\tag{12}
$$

in (10) is the kernel of the Rayleigh-Sommerfeld diffraction formula (see Eq. (3–36) of [54], and [53]), it represents the field produced at $\vec{r}_1 = (x_1, y_1, 0)$ due to a point source (scatterer) located at $\vec{r}_0 = (x_0, y_0, z_0)$. It is clear that if the transmission array beam, $\widetilde{\Phi}_{\text{Array}}^T(\vec{r}_0, \omega)$, is replaced with an arbitrary beam, (10) is still valid. The effects of the transmission beam and the object function, $f(\vec{r}_0)$, in (10) are to modulate the phase and amplitude of point sources at $\vec{r}_0$. This proves that the limited-diffraction array beam aperture weightings [24]–[26], [33]–[34] of echo signals (represented by $\widetilde{\Phi}_{\text{Array}}^R(\vec{r}_0, \omega)$) are identical to the 2-D spatial Fourier transform of the signals over the same transducer aperture, $\vec{r}_1$, even for an arbitrary transmission beam. Because an arbitrary transmission beam can always be expanded in terms of an array beam [14], [32], (10) or (8) can be used to reconstruct images for more complicated transmission schemes [54].

C. Limited-Diffraction Array Beam Imaging

The relationship between the Fourier transform of an object function and that of received echo signals ((8) and (9)) is very general and flexible in terms of image reconstructions. They include many methods developed previously: for example, (a) HFR imaging (plane wave transmission without steering, i.e., $k_{x_T} = k_{y_T} = 0$ in (9)) [24]–[25]; (b) two-way dynamic focusing (both $k_x = k_{x_T}$ and $k_y = k_{y_T}$ in (9) for multiple limited-diffraction array beam transmissions and receptions) [24], [26]; (c) multiple steered plane waves with the same steering angles in each plane-wave transmission and reception ($k_x = k_{x_T} = k \sin \zeta_T \cos \theta_T$ and $k_y = k_{y_T} = k \sin \zeta_T \sin \theta_T$ in (9), where ζ_T and θ_T are fixed in each transmission, and are the Axicon angle and the azimuthal angle of X waves, respectively) [35]; (d) steered plane waves (fixing ζ_T and θ_T in (5) and (9) in each transmission but varying k_x and k_y in image reconstructions, i.e., $k_{x_T} = k \sin \zeta_T \cos \theta_T$ and $k_{y_T} = k \sin \zeta_T \sin \theta_T$); and (e) limited-diffraction array beam imaging, where k_{x_T} and k_{y_T} in (9) are fixed in each transmission, but k_x and k_y are varied in image reconstructions [29]–[31]. In the last method, the following set of four limited-diffraction array beams [14], [32] for each pair of k_{x_T} and k_{y_T} are transmitted for 3-D imaging [29]–[32]:

$$
\begin{cases}
\Phi_{\text{Array}(1)}^T(\vec{r}_0, t) = \cos(k_{x_T} x_0) \cos(k_{y_T} y_0) \, G(z_0, t; k_{x_T}, k_{y_T}) \\
\Phi_{\text{Array}(2)}^T(\vec{r}_0, t) = \cos(k_{x_T} x_0) \sin(k_{y_T} y_0) \, G(z_0, t; k_{x_T}, k_{y_T}) \\
\Phi_{\text{Array}(3)}^T(\vec{r}_0, t) = \sin(k_{x_T} x_0) \cos(k_{y_T} y_0) \, G(z_0, t; k_{x_T}, k_{y_T}) \\
\Phi_{\text{Array}(4)}^T(\vec{r}_0, t) = \sin(k_{x_T} x_0) \sin(k_{y_T} y_0) \, G(z_0, t; k_{x_T}, k_{y_T})
\end{cases}
\tag{13}
$$

where

$$G\left(z_0, t; k_{x_T}, k_{y_T}\right) = \frac{1}{2\pi} \int\limits_{-\infty}^{\infty} A(k)H(k)e^{ik_{z_T} z_0}e^{-i\omega t}dk$$
$$= \Im_\omega^{-1}\left\{A(k)H(k)e^{ik_{z_T} z_0}/c\right\}, \quad (14)$$

and where $\Im_\omega^{-1}$ represents an inverse Fourier transform in terms of ω.

For every set of transmissions, one obtains four areas of coverage in the spatial Fourier domain of $f\left(\vec{r}_0\right)$, denoted as $\widetilde{R}^{(1)} = \widetilde{R}^{(1)}_{k'_x, k'_y, k'_z}(\omega)$, $\widetilde{R}^{(2)} = \widetilde{R}^{(2)}_{k'_x, k'_y, k'_z}(\omega)$, $\widetilde{R}^{(3)} = \widetilde{R}^{(3)}_{k'_x, k'_y, k'_z}(\omega)$, and $\widetilde{R}^{(4)} = \widetilde{R}^{(4)}_{k'_x, k'_y, k'_z}(\omega)$, respectively, from combinations of the four echo signals (see (8), and (15), next page).

From both (15) and (9), high-quality 3-D images that have an equivalent of dynamic focusing in both transmission and reception of the traditional D&S method [37] can be reconstructed. Varying the free parameters, k_{x_T} and k_{y_T}, from one set of transmissions to another, one obtains partially overlapped coverage of the spatial Fourier domain. Superposing the resulting partially reconstructed images in space or in their spatial Fourier domain from different transmissions, one obtains the final image. The superposition in the spatial domain can be done either coherently (increasing image resolution and contrast) or incoherently (reducing speckle). In the frequency domain, the superposition can be done only coherently, which, in theory, is equivalent to the superposition in the spatial domain. The superposition will also increase the field of view of the final image for transducers of a finite aperture [29]–[31].

In the case of 2-D imaging, (13) and (15) can be simplified by setting $k_y = k_{y_T} = 0$ (similar to Eq. (34) of [24]):

$$\begin{cases} \Phi^T_{\text{Array}(1)}\left(x_0, z_0, t\right) = \cos\left(k_{x_T} x_0\right) G_1\left(z_0, t; k_{x_T}\right) \\ \Phi^T_{\text{Array}(2)}\left(x_0, z_0, t\right) = \sin\left(k_{x_T} x_0\right) G_1\left(z_0, t; k_{x_T}\right) \\ F_{BL}\left(k_x + k_{x_T}, k'_z\right) = c^2 H(k)\left(\widetilde{R}^{(1)}_{k'_x, k'_z}(\omega) + i\widetilde{R}^{(2)}_{k'_x, k'_z}(\omega)\right) \\ F_{BL}\left(k_x - k_{x_T}, k'_z\right) = c^2 H(k)\left(\widetilde{R}^{(1)}_{k'_x, k'_z}(\omega) - i\widetilde{R}^{(2)}_{k'_x, k'_z}(\omega)\right) \end{cases},$$
$$(16)$$

where $G_1\left(z_0, t; k_{x_T}\right) = G\left(z_0, t; k_{x_T}, k_{y_T}\right)$ with $k_{y_T} \equiv 0$.

D. Square-Wave Aperture Weightings

A traditional imaging method such as D&S [37] requires a phase delay for each element of an array transducer to focus or steer a beam. The phase delay makes it difficult to share transmitters among transducer elements. As a result, a large number of transmitters are needed, especially for an array transducer that has many elements such as a 2-D array. Although the limited-diffraction array beam imaging method in (13) and (16) [29]–[31] may reduce the number of transmitters, it would still need a large number of transmitters to realize the exact sine and cosine aperture weightings.

The need of a large number of transmitters may cause problems. For example, modern transmitters are linear RF power amplifiers to accommodate the need of applications such as nonlinear imaging [40] and coded excitations [41]. To maintain good linearity over a broad bandwidth at a high output voltage, the transmitters may have high power consumption, and thus they must be physically large to dissipate heat and avoid short circuit. In addition, to produce exact sine and cosine weightings with an array transducer, each transducer element may need a complicated switching network to connect among a large number of transmitters between transmissions.

To reduce the number of transmitters, we develop the limited-diffraction array beam imaging with square-wave aperture weightings, in which the sine and cosine aperture weightings in (13) and (16) are approximated, respectively, with the following square-wave weighting functions:

$$w_s(x) = \begin{cases} 1, & \sin(x) \geq 0, \\ -1 & \sin(x) < 0 \end{cases}, \quad (17)$$

and

$$w_c(x) = \begin{cases} 1, & \cos(x) \geq 0, \\ -1 & \cos(x) < 0 \end{cases}. \quad (18)$$

If k_{x_T}, k_{y_T}, or both k_{x_T} and k_{y_T} in (13) and (16) are zero, the corresponding sine functions are set to zero; that is, these beams are not transmitted. With such an approximation, a 3-D imaging system may be developed with only two transmitters: one has an output voltage of a fixed amplitude, and the other has an inverted output from the first. Each transducer element is then connected to either one of the transmitters through an electronic switch that is controlled by a digital logic, depending on the sign of the sine and cosine functions at the position of the element. Combined with the computation efficiency of the FFT algorithm used in the HFR imaging method [24]–[26], simplified HFR and high-quality 3-D imaging systems can be constructed.

The square-wave aperture weightings can also be implemented with a single transmitter to further reducer the number of transmitters (removing the inverting transmitter and setting the negative weighting amplitude to zero). In this case, transducer elements are switched on or off to the single transmitter before each transmission, which may simplify the switching circuits. However, the direct current (DC) offset in the weighting functions needs to be compensated during the image reconstruction, which may require additional transmissions with a DC weighting that may reduce the image frame rate and complicate the signal processing, although the additional transmissions may be used to enhance the SNR for the center strip of the image. In addition, because about half of the transducer elements are not activated in each transmission (except for $k_{x_T} = k_{y_T} = 0$), the SNR of echo signals may be reduced.

It is worth noting that, because of the reciprocal relationship in (8), where $\Phi^R_{\text{Array}}\left(\vec{r}_0, t\right)$ and $\Phi^T_{\text{Array}}\left(\vec{r}_0, t\right)$ are

$$
\begin{cases}
F_{BL}\left(k_x + k_{x_T}, k_y + k_{y_T}, k_z'\right) = c^2 H(k)\left(\widetilde{R}^{(1)} + i\widetilde{R}^{(2)} + i\widetilde{R}^{(3)} - \widetilde{R}^{(4)}\right) \\
F_{BL}\left(k_x + k_{x_T}, k_y - k_{y_T}, k_z'\right) = c^2 H(k)\left(\widetilde{R}^{(1)} - i\widetilde{R}^{(2)} + i\widetilde{R}^{(3)} + \widetilde{R}^{(4)}\right) \\
F_{BL}\left(k_x - k_{x_T}, k_y + k_{y_T}, k_z'\right) = c^2 H(k)\left(\widetilde{R}^{(1)} + i\widetilde{R}^{(2)} - i\widetilde{R}^{(3)} + \widetilde{R}^{(4)}\right) \\
F_{BL}\left(k_x - k_{x_T}, k_y - k_{y_T}, k_z'\right) = c^2 H(k)\left(\widetilde{R}^{(1)} - i\widetilde{R}^{(2)} - i\widetilde{R}^{(3)} - \widetilde{R}^{(4)}\right)
\end{cases}
, \tag{15}
$$

exchangeable, the square-wave aperture weightings can also be applied to the reception beam forming to approximate the limited-diffraction array beam aperture weightings of echo signals [24]–[26], [33]–[34]. This may simplify the hardware needed to produce $R_{k_x+k_{x_T}, k_{y_T}, k_z+k_{z_T}}(t)$ in (8) for all k_x and k_y, given a pair of k_{x_T} and k_{y_T} in a transmission. For example, analog summation and subtraction amplifiers could be used to produce all of the required spatial frequency components at k_x and k_y in real time to replace some of high-speed FFT [55] circuits [42].

Although the square-wave aperture weighting method is general for both 2-D and 3-D imaging, for simplicity, in this paper only 2-D images will be reconstructed based on (16). In addition, the spatial Fourier transform of echo signals over transducer apertures in (10) will be used to speed up image reconstructions.

III. DEVELOPMENT OF THE HFR IMAGING SYSTEM

A. Imaging System Development

To experimentally study and further understand the high frame rate (HFR) imaging methods [24]–[27], [29]–[31], a general-purpose HFR imaging system was designed and constructed [38]–[39]. The successful construction of the system has helped to develop the method of limited-diffraction array beam imaging with square-wave aperture weightings in Section II.

The HFR imaging system was designed with the following basic requirements: (1) it is capable of recording RF data from each transducer element for at least one heart cycle synchronized to an electrocardiogram (ECG) signal at the maximum frame rate determined by the ultrasound propagation speeds in soft tissues and the system timing overhead; (2) the system has an independent linear power transmitter (amplifier) and an associated fast transmit/receive (T/R) switch for each transducer element; (3) RF data acquired are stored in the system and then transferred to a personal computer (PC) via a standard high-speed link such as a universal serial bus (USB) 2.0 (up to 480 Mb/s) for image reconstruction, and the system is controlled by the same PC; and (4) the system is flexible for various image reconstruction algorithms.

From the basic requirements, both the transmission and the reception circuits were designed to have 128 independent channels for an array transducer of 128 elements. The bandwidth of both the transmitter and receiver is
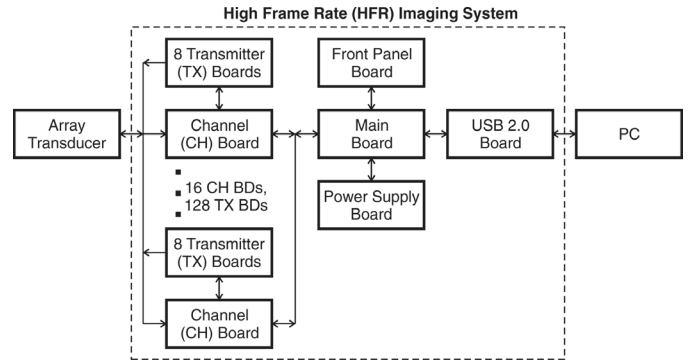

Fig. 2. Block diagram of the HFR imaging system. The dashed box indicates PCBs and components housed inside the enclosure of the HFR imaging system. The system consists of 6 different boards: (1) transmitter (TX) board, (2) channel (CH) board, (3) main board, (4) USB 2.0 board, (5) front panel board, and (6) power supply board. Each channel board contains 8 independent analog receiving channels and digital circuits that control 8 independent transmitters. There are 16 channel boards (128 channels) and 128 transmitter boards in total in the system. An array transducer is connected in front to send and receive ultrasound waves, and a PC is used to control the system and obtain RF data from each transducer element to reconstruct images.

about 10 MHz. The sampling frequency is 40 MHz and the quantization resolution is 12 bits for both analog-to-digital (A/D) and digital-to-analog (D/A) converters that are used to digitize echo signals and produce arbitrary transmission waveforms, respectively. Each receiving channel has a time-gain-control (TGC) amplifier and 64-MB synchronous random access memory (SDRAM) (up to 512 MB/channel) in a DIMM (dual in-line memory module) socket. The linear power amplifier in each channel is independent and is capable of driving a 75-ohm resistive load at up to ± 144 V peak voltage, producing an arbitrary waveform of a maximum length of 51.2 μs in each transmission and having an accuracy of 6.25 ns (160 MHz clock) in time delays. The system can be triggered by external sources such as an ECG machine, and it is able to trigger and synchronize external equipment. The system has a modular design with great redundancies built into the printed circuit boards (PCBs) so that each may be used independently without connecting to other PCBs. This will help to test new research ideas without redesigning the PCBs. To take advantage of the computing power of modern PCs and avoid obsoleteness, the system does not implement image reconstruction algorithms in hard-

ware. The system can be viewed as the arms and legs of a PC, through which users control the system by setting parameters on a graphical user interface (GUI) developed with Microsoft Visual C++. The system is capable of semi-real-time imaging using a loop command on the GUI. The speed of the loop depends mainly on that of image reconstructions of the PC.

It is a challenge to develop such a complicated medical imaging system in a university laboratory from scratch. This is because most students and postdocs are not experienced in high-frequency and high-power hardware. The system was proposed to the National Institutes of Health of the United States for funding in 1996; the development started in fall 1997 and lasted for several years after it was funded. The current design was based on field-programmable gate arrays (FPGAs) and was started in late 1999. The advantage of the FPGA-based design is that the hardware functions of the system can be upgraded through software without redesigning the circuits. Because of the fast pace of the advancement of digital electronics in industry, the system design has been improved several times to take advantage of the latest technologies. By July 2003, the system was partially constructed (see multimedia movies and animations showing the system construction) [39]. Further testing, troubleshooting, and improvement by redesigning some PCBs and reassembling components continued in 2004 [38]. The first *in vivo* image of a human heart was obtained on March 6, 2005, with the system and a custom-made 128-element transducer of 0.32-mm pitch and 3.5-MHz center frequency (see Section III-B below). During the course of the development of the HFR imaging system, dozens of small subsystems have also been developed for fast prototyping in the future [39]. It is worth noting that, currently, many imaging systems are capable of obtaining RF signals from particular beam formers or from transducer elements [56]–[60]. However, these systems are developed with different design philosophies or are tailored for specific applications.

Fig. 2 shows a block diagram of the HFR imaging system that consists of six types of PCBs (see the figure legend). There are 16 channel boards, each of which contains 8 receiving channels, for a total of 128 channels. There is one transmitter board for each channel. Commercial array transducers of up to 128 elements can be connected to the imaging system through various pin converters. A PC is used to control the system and receive data for image reconstructions. Photos of the completed HFR imaging system and the six types of PCBs are shown in Figs. 3 and 4, respectively. Surface-mount technology is used to construct PCBs. Multiple layers are used to improve signal integrity (reduce the radio-frequency interference and electromagnetic interference) and to accommodate complicated routing requirements (there are about 5,000 components with 15,000 pads for each channel board). Traces on the boards are at least 6 mils (6/1000 inches) wide to reduce costs. Block diagrams of the six types of PCBs are shown in Figs. 5–10, and the GUI used to control the system is shown in Fig. 11.
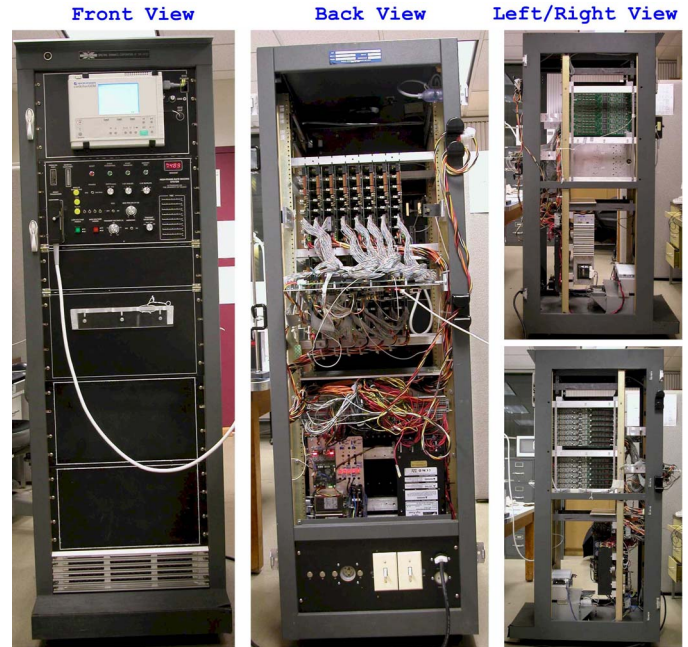

Fig. 3. Photos of the HFR imaging system showing the front (left), back (middle), left (right top), and right (right lower) views. The system is powered on. In the front view, there is a commercial Nihon Kohden (Nihon Kohden America, Inc., Foothill Ranch, CA) ECG-9020K 12-lead ECG machine (white instrument) that triggers the HFR imaging system to acquire images at a desired moment of a heart cycle. The front view also contains a standard 156-pin ITT Cannon (ITT Industries, Cannon, Santa Ana, CA) connector for array transducers (connected through a thick white cable). The back and side views show how PCBs and components are arranged and interconnected. (Modified from Fig. 1 of [38].)

B. Safety of the HFR Imaging System for In Vivo Experiments

One of the primary applications of the HFR imaging system is for *in vivo* imaging of humans. This raises concerns of the safety of the system. Hence, the imaging system was tested with the parameters defined in [43]–[45] for two 1-D-array transducers used in the experiments. The first is custom-made and has 128 elements, and a center frequency and −6 dB pulse-echo bandwidth of 3.5 MHz and 50%, respectively. The width is 8.6 mm in elevation dimension without elevation focus and the pitch is 0.32 mm, that is, about 3/4 of the center wavelength of the transducer in water. The second transducer is an Acuson V2 phased array, with 128 elements, a 0.15-mm pitch, a 2.5-MHz center frequency, and a 14-mm elevation aperture focused at 68 mm.

The MI, TI (only the soft-tissue thermal index (TIS) is considered in this paper for the intended applications of the system), and AO or $I_{\text{SPTA.3}}$ [43]–[45] were measured for these transducers. The MI is defined as (see Eq. (1) of [43])

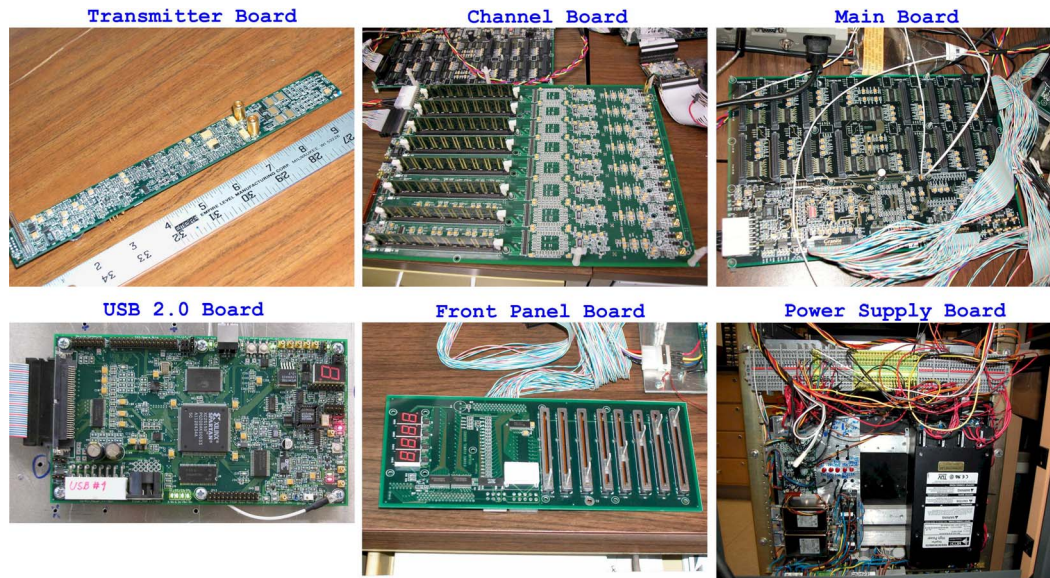$$\text{MI} = \frac{P_{\text{r.3}}/f_{\text{awf}}^{1/2}}{C_{\text{MI}}}, \tag{19}$$

Fig. 4. Photos of the six types of PCBs described in Fig. 2: (1) transmitter board (top left): 6 layers and 9.7 inches × 1.2 inches in dimensions, (2) channel board (top middle): 8 layers and 11 inches × 8 inches in dimensions, (3) main board (top right): 6 layers and 12 inches × 8 inches in dimensions, (4) USB 2.0 board (bottom left): 4 layers and 7 inches × 4 inches in dimensions, (5) front panel board (bottom middle): 4 layers and 9.76 inches × 4 inches in dimensions, and (6) power supply board (bottom right): 4 layers and 5 inches × 3 inches in dimensions. The power supply board (on the middle-left side of the panel) is mounted on a rack with other power supply units and components. Part of the wiring from the power supplies can be seen. (Modified from Figs. 2, 3, 5, 7, and 8 of [38].)
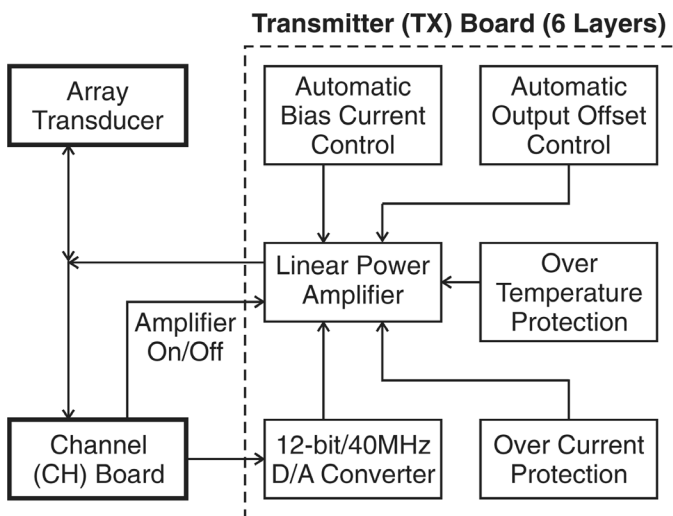
Fig. 5. Block diagram of a transmitter board shown in Figs. 2 and 4. The dashed box indicates circuit components on the board. The interaction of the board with other parts of the system is also shown. The linear amplifier is designed to produce broadband (0.05 to 10 MHz) arbitrary waveforms (with a 40-MHz 12-bit D/A converter) of a maximum output up to ±144 V peak voltage at a 75-ohm resistive load. To reduce the static power consumption and nonlinear distortions, the bias current and the offset voltage of the transmitter are automatically controlled and adjusted [38]. The amplifier is also protected from output shortage and equipped with an over-temperature shutdown circuit.
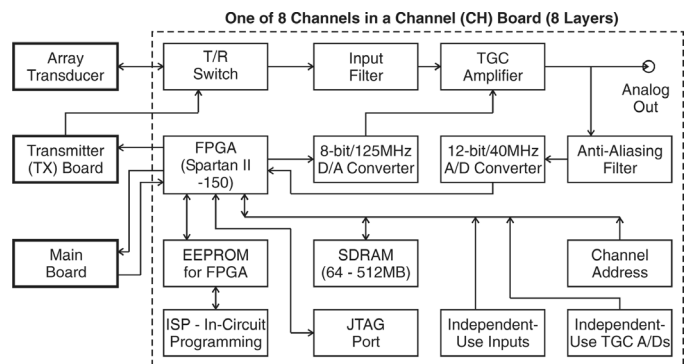

Fig. 6. Block diagram of one of the 8 channels on a channel board shown in Figs. 2 and 4. The dashed box and its interaction with other parts of the system are similar to those of Fig. 5. The channel has a standard low-noise, high-gain (108 dB), and broadband (−6 dB bandwidth of about 0.25 to 10 MHz) TGC analog front end with a 40-MHz, 12-bit A/D converter. Buffered analog output is available. The channel is controlled by an FPGA (Xilinx Spartan II - 150, Xilinx, Inc., San Jose, CA). The FPGA is interfaced to 64–512-MB SDRAM and is capable of in-system programming (ISP). Data can be sent to and from the main board via cables. Each channel board can also be used independently without the main board, meaning it can be used as an 8-channel analog pulser/receiver with an 8-segment TGC control (via an 8-channel 2-MS/s A/D converter), pulse inversion for harmonic imaging, time delays for beam steering and focusing, preprogrammed transmission waveforms, and TGC depth selections. The EEPROM, ISP, and JTAG components are used for different ways of FPGA programming.
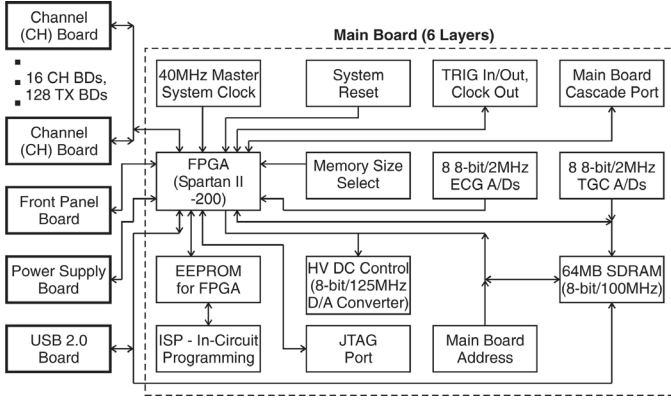
Fig. 7. Block diagram of the main board shown in Figs. 2 and 4. The dashed box and its interaction with other parts of the system are similar to those of Fig. 5. The FPGA (Xilinx Spartan II - 200) and its programming components have functions similar to those in Fig. 6. This board contains a 40-MHz master clock and interacts with most parts of the system. The main board can be cascaded (using its address to distinguish between boards) with other main boards to increase the number of channels beyond 128. The board has a 64-MB SDRAM to hold configuration data sent from a PC. An 8-bit/125-MHz D/A converter can be used for multiple purposes in addition to trimming up/down the high voltages applied to the transmitters. Memory size selector indicates the size of installed memory in the channel boards (in one of the following sizes: 64, 128, 256, or 512 MB/channel). Two 8-channel 2-MHz A/D converters are used to digitize TGC levels and the ECG signal, among other uses. The system can be controlled and synchronized by external equipments, or vice versa, through the TRIG IN/OUT and CLOCK IN/OUT interface. Multiple system reset mechanisms are available through the front panel, the on-board push button, and the PC.

where $C_{MI} = 1$ MPa MHz$^{1/2}$, $P_{r.3}$ is the attenuated peak-rarefactional pressure in MPa, and f_{awf} is the acoustic working frequency in MHz. The subscript ".3" represents 0.3 dB/MHz/cm attenuated values (notice that the dB definition for pressure and power is different). The TI, specifically TIS, in scanned mode for soft tissue at the surface of transducer is given by (see Eqs. (2) and (11) of [43])

$$TI = TIS = \frac{W_p}{W_{deg}} = \frac{W_{01} f_{awf}}{C_{TIS1}}, \qquad (20)$$

where W_p is the power parameter, W_{deg} is the estimated power necessary to raise the temperature of the target tissue by $1°C$, W_{01} (mW) is the acoustic power bounded by 1-cm soft tissue perfusion length, and $C_{TIS1} = 210$ mW·MHz is a constant. The AO is defined as [43]

$$AO = I_{SPTA.3} = \max_{\forall (x,y)} \left\{ f_{pr} \int_{t_1}^{t_2} \frac{P_{.3}^2(\vec{r};t)}{\rho c} dt \right\} \Bigg|_{z=\text{constant}}, \qquad (21)$$

where $P_{.3}(\vec{r};t)$ is the attenuated pressure at the position $\vec{r} = (x,y,z)$ and time t; z is the distance from the transducer and is a constant at a given depth; f_{pr} is the pulse repetition frequency (in calculation of Table I, a non-scanned mode such as Doppler was assumed to obtain the highest values of AO); $\max_{\forall (x,y)} \{\cdot\}$ means to find a peak value
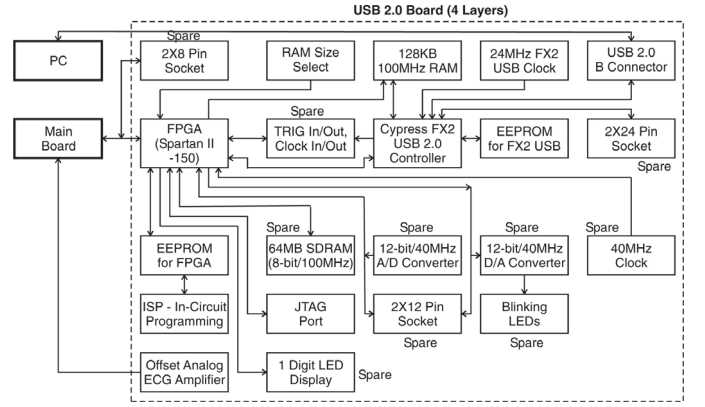

Fig. 8. Block diagram of the USB 2.0 board shown in Figs. 2 and 4. The dashed box and its interaction with other parts of the system are similar to those of Fig. 5. The FPGA (Xilinx Spartan II - 150) and its programming components have functions similar to those in Fig. 6. The main function of the board is to provide a USB 2.0 (up to 480 Mbits/s) interface between the imaging system and a PC. The function is implemented with a Cypress FX2 chip (San Jose, CA) that contains an 8051 microcontroller running with 128 KB RAM. A 512-Kbit EEPROM is used to store the program (firmware) of the 8051 microcontroller. The FX2 runs with a 24-MHz clock that is different from that of the 40-MHz system master clock. The board contains spare components (see the word "spare" near the components) so that it can be easily used as an independent high-speed (40 MHz) and high-resolution (12-bit) A/D and D/A converter with an on-board 64-MB memory and with the ability to synchronize or be synchronized with external equipment through its TRIG IN/OUT and CLOCK IN/OUT circuits. Spare header sockets make it easier to connect the board with external circuits. The offset analog ECG amplifier is used for the ECG A/D on the main board. The one-digit light emitting diode (LED) can be used for the diagnosis of the FPGA or 8051 microcontroller program and for board status display.
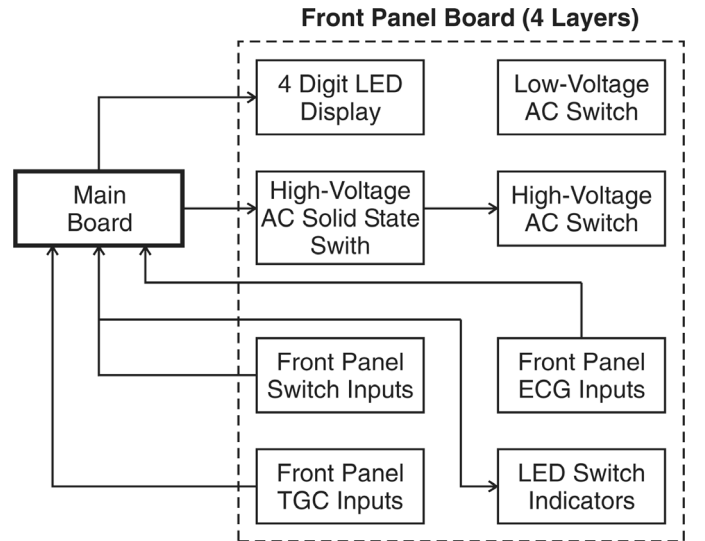

Fig. 9. Block diagram of the front panel board shown in Figs. 2 and 4. The dashed box and its interaction with other parts of the system are similar to those of Fig. 5. The board interacts with the front panel switches and buttons to accept commands and display the status of the HFR imaging system using a 4-digit LED panel. The front panel inputs include 8 TGC setting potentiometers, ECG on/off, ECG delay setting, system reset, system commands, system functions, low-voltage and high-voltage power on/off switches, and solid state on/off switch for high-voltage power that is controllable via a PC. Each switch or button is associated with an LED indicator.

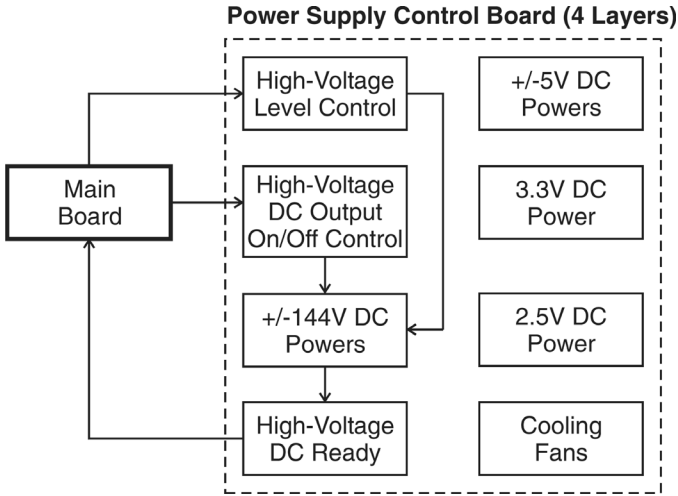**Power Supply Control Board (4 Layers)**

Fig. 10. Block diagram of the power supply board shown in Figs. 2 and 4. The dashed box and its interaction with other parts of the system are similar to those of Fig. 5. The board interacts with the main board to turn on/off DC outputs and adjust the DC output level of the ± 144 V high-voltage power supplies via a PC. The board also detects whether the high-voltage DC level has reached desired values so that the main board can start to issue data acquisition commands. In addition to the high-voltage power supplies, the system has several low-voltage power supplies (± 5, 3.3, and 2.5 V). Fans are installed to cool the system.

for all x and y at the depth z; ρ and c are the density and the speed of sound of the tissue, respectively; and t_1 and t_2 are the time before the beginning and after the end of the pulse, respectively (i.e., $t_2 - t_1$ is the time interval over which the envelope of the pulse is not zero).

In the measurement, one-cycle sine wave pulses at the respective center frequencies of the transducers were used. A pulse repetition period of 187 μs (5348 transmissions/s) was applied and the high-voltage power supplies were limited to ± 96 V peak. Two imaging conditions were considered. One is for the standard D&S method where transmit beams are focused at different depths. The other is for the 2-D and 3-D HFR imaging [24]–[26], where a plane-wave type of transmit beams is used. The HFR imaging system was synchronized with a three-axis scanning system driven by stepper motors of up to 0.2 μm translation per step. Ultrasound fields in distilled water were measured across the entire beam areas along both the transverse and the elevation directions of the transducers at various depths with a factory-calibrated needle hydrophone (NTR Systems, Inc., Seattle, WA) of a 0.6-mm diameter and 25-μm thickness. Signals were digitized with a 12-bit Gage CS12100 computer card (Gage Applied Sciences, Inc., Montreal, Quebec, Canada) at the 40-MHz clock of the HFR imaging system. Results are shown in Table I.

In *in vivo* experiments, the Acuson V2 transducer with a 68-mm elevation focal distance was used. Furthermore, only beams focused at 70-mm distance were used for D&S imaging. The upper U.S. Food and Drug Administration (FDA) limits of the MI and AO are 1.9 and 720 mW/cm^2, respectively [43]–[45]. Therefore, it is clear from Table I that our system is operating under the FDA limits for the

HFR imaging related methods (using a plane-wave type of transmissions) and at about the limits with the D&S method. Table I also shows that the conventional D&S method may exceed the FDA limits as the focal distance of the transmission beam is decreased. For the HFR imaging related methods, the highest MI, TI, and AO occur near the surface of the transducer (notice that the elevation focus of the Acuson V2 probe moves the highest MI and AO a small distance away from the surface). The TI values in Table I indicate that there could be over 3.6°C increase in temperature at the surface of the transducer. However, we did not feel it in the experiments. This could be due to the conservative estimation of the perfusion length of 1 cm used in the calculation.

The table also makes it clear that more power could be allowed for the HFR imaging related methods without exceeding the FDA limits on the MI and AO, as compared to the conventional D&S method. This may increase the SNR of the HFR imaging-related methods. This is because, as mentioned before, for a plane-wave type of transmission beams such as limited-diffraction array beams with square-wave aperture weightings and steered plane waves, the highest MI, TI, and AO occur at the surface of the transducers due to tissue attenuation, which is not the case for a tightly focused beam of the conventional D&S method. Because the MI is proportional to the peak rarefaction pressure and is capped at 1.9 by the FDA [43], a higher surface pressure (or more total transmission energy) could be allowed for a plane-wave type of beam than for a focused beam to increase the SNR. Nevertheless, to ensure human safety, the American Institute of Ultrasound in Medicine (AIUM) suggests following the ALARA (as low as reasonably achievable) principle [43]–[45], that is, a principle that mandates that ultrasound exposure (in terms of the MI, TI, and exposure time) be kept "as low as reasonably achievable" without compromising diagnostic capability or resolution.

IV. IN VITRO AND IN VIVO EXPERIMENTS AND RESULTS

Both *in vitro* and *in vivo* experiments were performed for the limited-diffraction array beam imaging with square-wave aperture weightings using the high frame rate (HFR) imaging system [38]–[39].

In the *in vitro* experiments, the custom-made 3.5-MHz transducer was used to transmit a one-cycle sine wave pulse at the center frequency. Echo signals were digitized at 40 MHz but were down-sampled to 10 MHz to reduce computation without compromising image quality. (The down sampling was performed for both the limited-diffraction array beam and the steered plane wave imaging methods, but not for the D&S imaging where the image quality is sensitive to the phase accuracy of the echo signals [29]–[31].) Images were reconstructed with (16) where the maximum k_{x_T} was determined by $k_{x_T\text{-max}} = \pi/\Delta x_1$, and where Δx_1 was the pitch of the transducer [29]–[31].
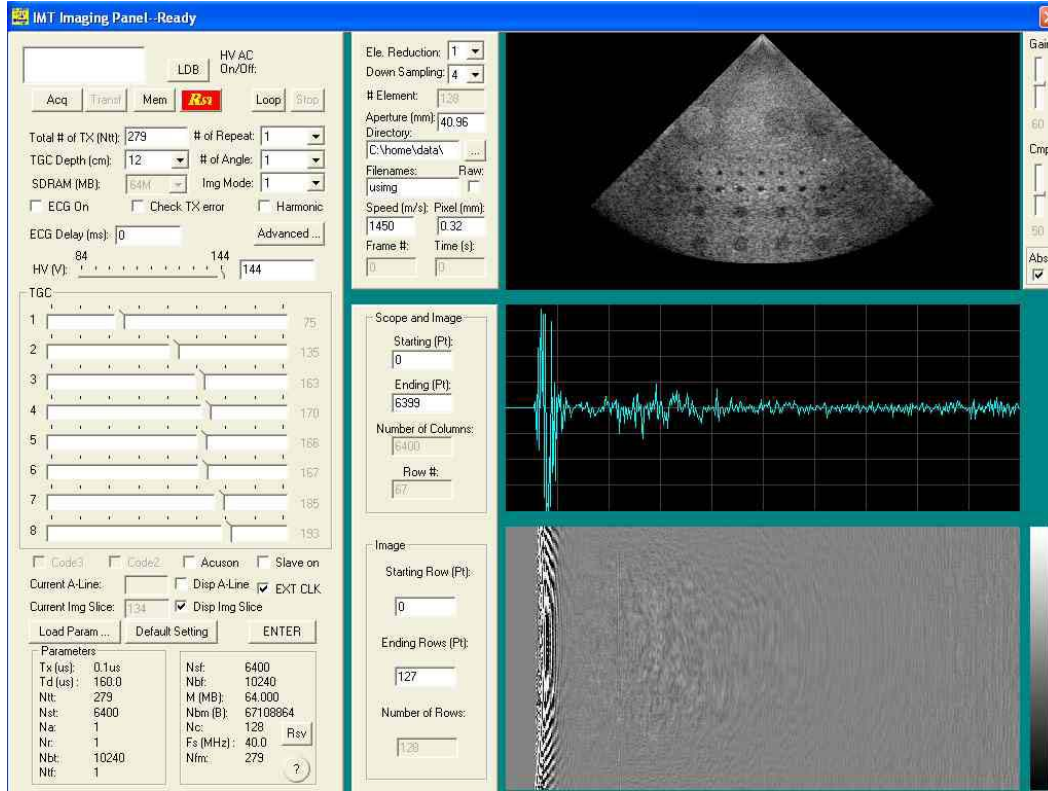
Fig. 11. Graphical user interface (GUI) written in Microsoft Visual C++ and run on the Microsoft Windows XP operating system to control the HFR imaging system. Parameters set on the GUI are sent to the system and the echo data acquired are sent back to the PC via the USB 2.0 link. The system works as if it were the arms and legs of the PC. The image shown was a thumbnail for preview only and was obtained with a 0.32-mm pitch, 3.5-MHz center frequency, and 128-element custom-made transducer electronically steered at ±45° and focused at a depth of 70 mm. A one-cycle sine wave was used in transmission, and 279 transmissions were used to reconstruct the image with the conventional D&S method of a dynamically focused reception. The three display panels on the right hand side of the GUI show the reconstructed image (top), oscilloscope display of a selected RF A-line (middle), and RF A-lines from all transducer elements obtained from one transmission (bottom). The loop function shown at the upper left panel allows the system to work in semi-real time. (A newer version than Figs. 10–12 of [38])

This translates $k_{x_T\_max}$ into a maximum equivalent steering angle of about ±40.34° at the center frequency of the transducer (notice that $k_{x_T} = k\sin\zeta_T$ for $\theta_T = 0$ in (5) and $c = 1450$ m/s). To obtain images, k_{x_T} was varied evenly from 0 to $k_{x_T\_max}$ to produce multiple limited-diffraction array beams. At each k_{x_T}, the square-wave aperture weightings corresponding to both the sine and cosine functions were applied (see (17) and (18)).

Results for wire and anechoic cylindrical targets of an ATS 539 tissue-mimicking phantom are shown in Figs. 12 and 13, respectively. It is clear that there is almost no difference between the images reconstructed with the exact (sine and cosine) and the square-wave aperture weightings, except that the latter has a higher SNR (deeper penetration) due to increased transmission power. In addition, since the square-wave aperture weightings need only one or two transmitters to obtain images, imaging systems may be simplified greatly, especially for future 3-D imaging where a large number of independent transducer elements may be used.

Results of *in vivo* experiments of the heart of a volunteer using the 2.5-MHz Acuson V2 transducer are shown in Fig. 14 and in the supplementary video. The experimental conditions were the same as those of the *in vitro* experiments except for the center-frequency and dimensions of the transducer.

In the *in vivo* experiments, a commercial Acuson 128XP/10 imaging system was used to find the position of interest of the heart. After the position was found, the transducer was unplugged from the Acuson system and then plugged into the HFR imaging system for data acquisition. To compare the new imaging method with existing methods, the HFR imaging system was programmed to transmit in the order of steered plane waves (SPW) (11, 19, and 91 transmissions (TXs)) [29]–[31], beams focused at 70 mm for D&S imaging (91 transmissions), and limited-diffraction array beams (LDB) with square-wave aperture weightings (91, 19, and 11 transmissions). This resulted in seven images showing successive phase delays of the heart in the sequence of panels (f) (SPW with 11 TXs), (e) (SPW with 19 TXs), (d) (SPW with 91 TXs), (g) (D&S with dynamic receive focusing with 91 TXs), (a) (LDB with 91 TXs), (b) (LDB with 19 TXs), and (c) (LDB with 11 TXs), respectively, with a field of view of
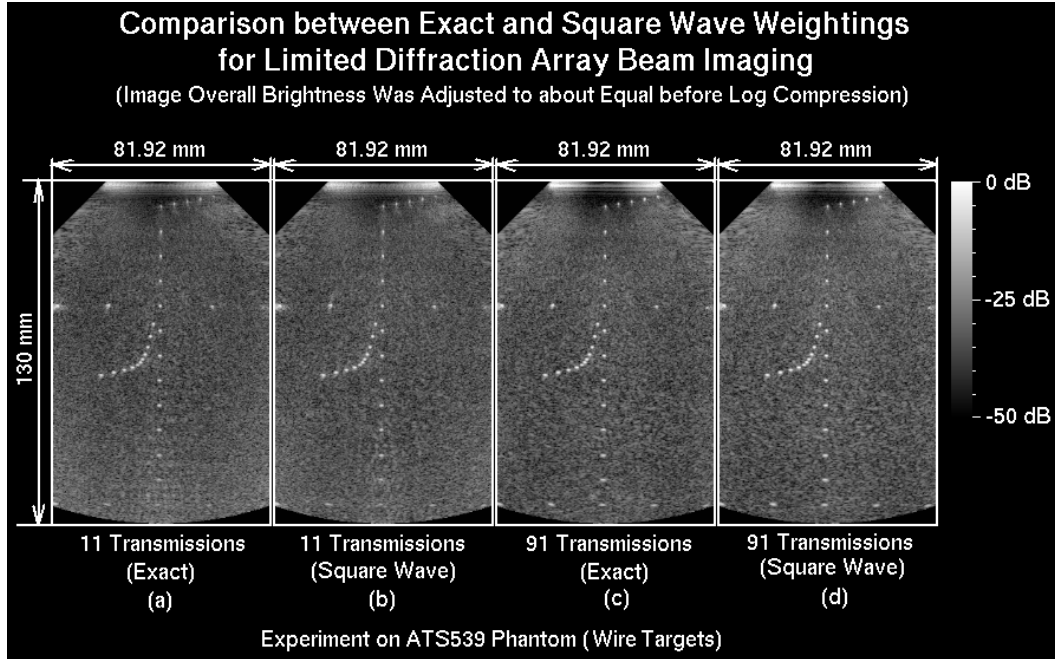
Fig. 12. Reconstructed images of wire targets of an ATS 539 tissue-mimicking phantom with the limited-diffraction array beam method. Images are log-compressed with a dynamic range of 50 dB. The speed of sound of the phantom is about 1450 m/s. Images of the exact aperture weightings ((a) and (c)) are compared with those with the square-wave weightings ((b) and (d)), respectively. Images in the left and right two panels were obtained with 11 (up to 507 frames/s with 1450 m/s speed of sound) and 91 transmissions (up to 61 frame/s), respectively. The field of view of the images is larger than $\pm 45°$ over a 130-mm depth.
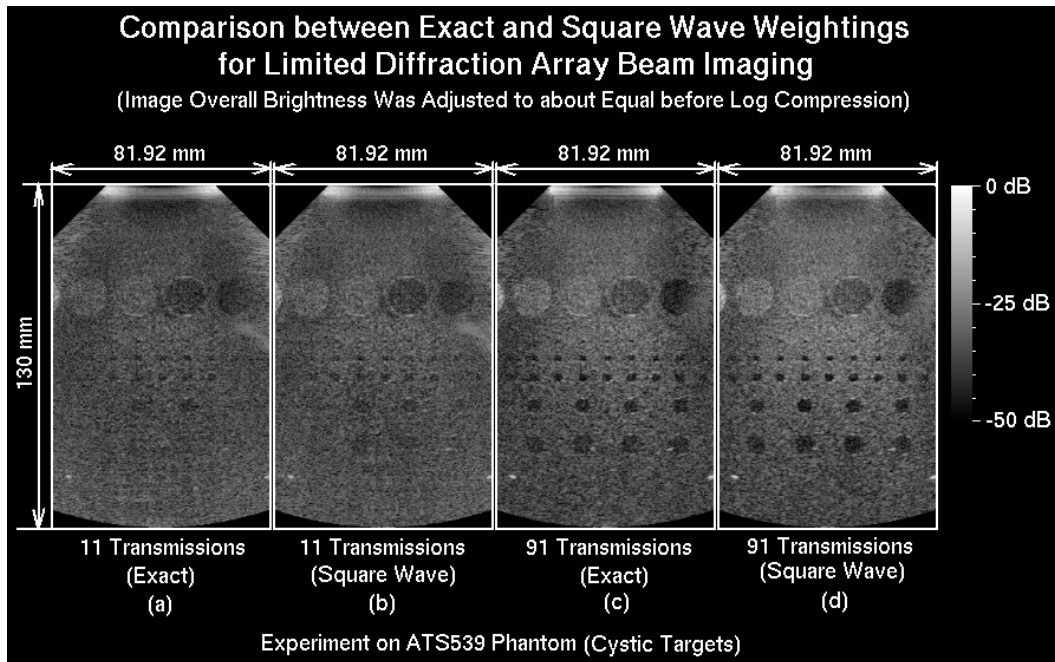

Fig. 13. This figure is the same as Fig. 12 except that images of the cystic and grayscale targets of the ATS 539 tissue-mimicking phantom were obtained.
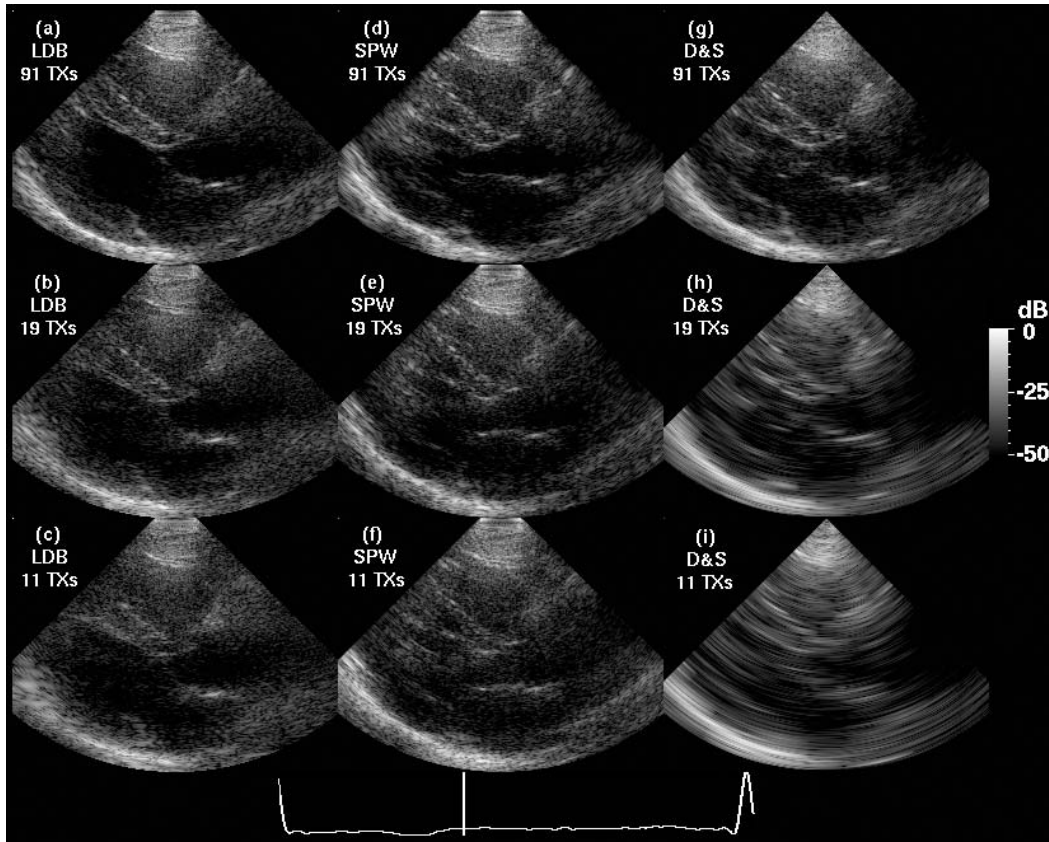
Fig. 14. *In vivo* heart images of a volunteer for comparison between the limited-diffraction array beam imaging with square-wave aperture weightings (panels (a), (b), and (c)) and other imaging methods (steered plane waves in panels (d), (e), and (f), and the D&S method with a fixed transmission focus at 70 mm and a dynamically focused reception in panels (g), (h), and (i)). Panels in the top, middle, and bottom rows correspond to the conditions of 91 (59 frame/s with 187 μs between transmissions), 19 (281 frames/s), and 11 (486 frames/s) transmissions to reconstruct a frame of image, respectively. Images are log-compressed with a dynamic range of 50 dB. The ECG at the bottom of the figure was obtained from the same volunteer. The vertical bar in the ECG indicates the starting moment when the series of images in this figure were acquired (this was roughly the moment of a rapid ventricular filling that pushed the mitral valve open quickly).

about 90° ($\pm 45°$) for each image (Fig. 14). (The field of view of both the SPW and the LDB imaging is slightly larger than that of D&S because a strip, instead of a line, of the image is reconstructed from each transmission. In the steered plane wave imaging, the steering angles were evenly spaced from $-\zeta_{T\_max}$ to ζ_{T_max}, where $\zeta_{T\_max} = 45°$, and in the D&S imaging, the steering angles were chosen in such a way that their sine values were evenly spaced from $-\sin\zeta_{T\_max}$ to $\sin\zeta_{T\_max}$ [29]–[31]. For limited-diffraction array beam imaging, $k_{x_T\_max}$ was calculated using $k_{x_T\_max} = k_c \sin\zeta_{T\_max} \leq \pi/\Delta x_1$, where $\Delta x_1 = 0.15$ mm and $k_c = 2\pi f_c/c$, and where $f_c = 2.5$ MHz and $c = 1540$ m/s.) The image depth is 120 mm and the pulse repetition period is 187 μs, which is the shortest allowed by the imaging system at this depth. This results in frame rates of 486, 281, and 59 frames/s for 11, 19, and 91 transmissions, respectively. The group of transmissions ($2 \times 11 + 2 \times 19 + 3 \times 91 = 333$ per group) above was repeated 18 times to cover an entire heart cycle with 5994 transmissions in total, lasting about 1.12 seconds.

From Fig. 14, it is clear that images obtained with the square-wave aperture weightings agree well with those obtained with the methods of both the steered plane waves

and the conventional D&S with a fixed transmission focal distance of 70 mm but with a dynamic receive beam forming. As a comparison, for the D&S method, 19 and 11 transmissions were extracted evenly from the 91 transmissions over a $\pm 45°$ angle, and images were reconstructed with bilinear interpolations and are shown in Fig. 14(h) and (i), respectively. These images show that for the D&S method, when the number of transmissions is reduced (frame rate is increased) while keeping the same 90° field of view, the quality of images degrades much faster than that of the HFR imaging-related methods.

To show a cycle of the heartbeat, an animation (▤) looping through the 18 groups of images (Fig. 14 shows Group #8 that has the fastest motion of the mitral valve) was produced with a time lag of about 0.06 seconds between neighboring groups. The animation is in a Quick-Time (Apple Computer, Inc., Cupertino, CA) format. In addition to the *in vivo* imaging of the heart in Fig. 14 and the supplementary video ▤, a preliminary study of the effects of motion on the HFR imaging related methods has been carried out [61], [62]. Results show that the HFR imaging methods are not sensitive to motion unless the number of transmissions is large (lower frame rate) and

the depth is small. Effects of phase aberration and noise on the HFR imaging related methods have also been studied and the results show that the effects are similar to those on the conventional D&S method [63].

V. CONCLUSION

A general-purpose high-frame rate (HFR) medical imaging system has been developed [38]–[39]. It works well and is an indispensable tool for the ultrasound research. It has been used to develop the square-wave aperture weighting method that is capable of reconstructing high-quality images (equivalent dynamic focusing in both transmission and reception) over a large field of view even for a fast moving object such as the heart with only one or two transmitters, which may simplify the transmission subsystem of an imager. The method may allow a higher total energy (or surface sound pressure) to be transmitted to increase the SNR than the traditional focused beam methods [37] without exceeding the upper limits of some safety parameters set by the FDA [43]–[45]. Due to the reciprocal principle, the method can also be applied to process echo signals in reception, which may further simplify the systems [42]. In addition, the theory leading to the development of the square-wave aperture weighting method shows that the relationship between the limited-diffraction array-beam aperture weightings in reception and a 2-D Fourier transform over the same aperture for a limited-diffraction array beam transmission [29]–[31] can be generalized to an arbitrary transmission beam. This provides an alternative approach for image reconstructions and may help to develop new imaging methods in the future.

ACKNOWLEDGMENTS

REFERENCES

[1] J. A. Stratton, *Electromagnetic Theory*. New York and London: McGraw-Hill Book Company, 1941, p. 356.

[2] J. Durnin, "Exact solutions for nondiffracting beams. I. The scalar theory," *J. Opt. Soc. Amer. A*, vol. 4, no. 4, pp. 651–654, 1987.

[3] J. Durnin, J. J. Miceli, Jr., and J. H. Eberly, "Diffraction-free beams," *Phys. Rev. Lett.*, vol. 58, no. 15, pp. 1499–1501, Apr. 1987.

[4] J.-y. Lu and J. F. Greenleaf, "Theory and acoustic experiments of nondiffracting X waves," in *Proc. IEEE Ultrason. Symp.*, vol. 2, 1991, pp. 1155–1159.

[5] J.-y. Lu and J. F. Greenleaf, "Nondiffracting X waves—Exact solutions to free-space scalar wave equation and their finite aperture realizations," *IEEE Trans. Ultrason., Ferroelect., Freq. Contr.*, vol. 39, no. 1, pp. 19–31, Jan. 1992.

[6] J.-y. Lu and J. F. Greenleaf, "Experimental verification of nondiffracting X waves," *IEEE Trans. Ultrason., Ferroelect., Freq. Contr.*, vol. 39, no. 3, pp. 441–446, May 1992.

[7] J.-y. Lu and A. Liu, "An X wave transform," *IEEE Trans. Ultrason., Ferroelect., Freq. Contr.*, vol. 47, no. 6, pp. 1472–1481, Nov. 2000.

[8] J.-y. Lu, H. Zou, and J. F. Greenleaf, "A new approach to obtain limited diffraction beams," *IEEE Trans. Ultrason., Ferroelect., Freq. Contr.*, vol. 42, no. 5, pp. 850–853, Sep. 1995.

[9] J.-y. Lu and J. F. Greenleaf, "Pulse-echo imaging using a non-diffracting beam transducer," *Ultrasound Med. Biol.*, vol. 17, no. 3, pp. 265–281, May 1991.

[10] J.-y. Lu and J. F. Greenleaf, "Ultrasonic nondiffracting transducer for medical imaging," *IEEE Trans. Ultrason., Ferroelect., Freq. Contr.*, vol. 37, no. 5, pp. 438–447, Sep. 1990.

[11] J.-y. Lu, T. K. Song, R. R. Kinnick, and J. F. Greenleaf, "In vitro and in vivo real-time imaging with ultrasonic limited diffraction beams," *IEEE Trans. Med. Imag.*, vol. 12, no. 4, pp. 819–829, Dec. 1993.

[12] J.-y. Lu and J. F. Greenleaf, "Evaluation of a nondiffracting transducer for tissue characterization," in *Proc. IEEE Ultrason. Symp.*, vol. 2, 1990, pp. 795–798.

[13] J.-y. Lu and J. F. Greenleaf, "Producing deep depth of field and depth-independent resolution in NDE with limited diffraction beams," *Ultrason. Imag.*, vol. 15, no. 2, pp. 134–149, Apr. 1993.

[14] J.-y. Lu, "Improving accuracy of transverse velocity measurement with a new limited diffraction beam," in *Proc. IEEE Ultrason. Symp.*, vol. 2, 1996, pp. 1255–1260.

[15] J.-y. Lu, X.-L. Xu, H. Zou, and J. F. Greenleaf, "Application of Bessel beam for Doppler velocity estimation," *IEEE Trans. Ultrason., Ferroelect., Freq. Contr.*, vol. 42, no. 4, pp. 649–662, July 1995.

[16] J.-y. Lu and J. Cheng, "Field computation for two-dimensional array transducers with limited diffraction array beams," *Ultrason. Imag.*, vol. 27, no. 4, pp. 237–255, Oct. 2005.

[17] J.-y. Lu and S. He, "Optical X wave communications," *Opt. Commun.*, vol. 161, pp. 187–192, March 15, 1999.

[18] J.-y. Lu, J. Cheng, and B. Cameron, "Low sidelobe limited diffraction optical coherence tomography," in *Proc. SPIE*, vol. 4619, 2002, pp. 300–311.

[19] C. Conti and S. Trillo, "Nonspreading wave packets in three dimensions formed by an ultracold Bose gas in an optical lattice," *Phys. Rev. Lett.*, vol. 92, p. 120404, 2004.

[20] P. Di Trapani, G. Valiulis, A. Piskarskas, O. Jedrkiewicz, J. Trull, C. Conti, and S. Trillo, "Spontaneously generated X-shaped light bullets," *Phys. Rev. Lett.*, vol. 91, p. 093904, 2003.

[21] C. Day, "Intense X-shaped pulses of light propagate without spreading in water and other dispersive media," *Phys. Today*, vol. 57, no. 10, pp. 25–26, Oct. 2004.

[22] J.-y. Lu, H. Zou, and J. F. Greenleaf, "Biomedical ultrasound beam forming," *Ultrasound Med. Biol.*, vol. 20, no. 5, pp. 403–428, July 1994.

[23] J.-y. Lu and J. F. Greenleaf, "Diffraction-limited beams and their applications for ultrasonic imaging and tissue characterization," in *Proc. SPIE*, vol. 1733, 1992, pp. 92–119.

[24] J.-y. Lu, "2D and 3D high frame rate imaging with limited diffraction beams," *IEEE Trans. Ultrason., Ferroelect., Freq. Contr.*, vol. 44, no. 4, pp. 839–856, July 1997.

[25] J.-y. Lu, "Experimental study of high frame rate imaging with limited diffraction beams," *IEEE Trans. Ultrason., Ferroelect., Freq. Contr.*, vol. 45, no. 1, pp. 84–97, Jan. 1998.

[26] J.-y. Lu, "Transmit-receive dynamic focusing with limited diffraction beams," in *Proc. IEEE Ultrason. Symp.*, vol. 2, 1997, pp. 1543–1546.

[27] G. Wade, "Human uses of ultrasound: Ancient and modern," *Ultrasonics*, vol. 38, pp. 1–5, 2000.

[28] J.-y. Lu and Z. Wang, "Blood flow velocity vector imaging with high frame rate imaging methods," in *Proc. IEEE Ultrason. Symp.*, 2006, to be published.

[29] J.-y. Lu and J. Cheng, "System for extended high frame rate imaging with limited diffraction beams," U.S. Patent filed.

[30] J. Cheng and J.-y. Lu, "Fourier based imaging method with steered plane waves and limited-diffraction array beams," in *Proc. IEEE Ultrason. Symp.*, vol. 2, 2005, pp. 1976–1979.

[31] J. Cheng and J.-y. Lu, "Extended high frame rate imaging method with limited diffraction beams," *IEEE Trans. Ultrason., Ferroelect., Freq. Contr.*, vol. 53, no. 5, pp. 880–899, May 2006.

[32] J.-y. Lu, "Limited diffraction array beams," *Int. J. Imaging Syst. Technol.*, vol. 8, no. 1, pp. 126–136, Jan. 1997.

[33] J.-y. Lu and S. He, "Increasing field of view of high frame rate ultrasonic imaging," *J. Acoust. Soc. Amer.*, vol. 107, no. 5, pt. 2, p. 2779, May 2000 (abstract).

[34] J.-y. Lu, "Nonlinear processing for high frame rate imaging," *J. Ultrasound Med.*, vol. 18, no. 3 (Supplement), p. S50, Mar. 1999 (abstract).

[35] M. Soumekh, "Array imaging with beam-steered data," *IEEE Trans. Image Processing*, vol. 1, no. 3, pp. 379–390, July 1992.

[36] H. Peng and J.-y. Lu, "High frame rate 2D and 3D imaging with a curved or cylindrical array," in *Proc. IEEE Ultrason. Symp.*, vol. 2, 2002, pp. 1725–1728.

[37] B. D. Steinberg, "Digital beamforming in ultrasound," *IEEE Trans. Ultrason., Ferroelect., Freq. Contr.*, vol. 39, no. 6, pp. 716–721, Nov. 1992.

[38] J.-y. Lu and J. L. Waugaman, "Development of a linear power amplifier for high frame rate imaging system," in *Proc. IEEE Ultrason. Symp.*, vol. 2, 2004, pp. 1413–1416.

[39] J.-y. Lu, "A multimedia example," *IEEE Trans. Ultrason., Ferroelect., Freq. Contr.*, vol. 50, no. 9, p. 1078, Sep. 2003.

[40] M. A. Averkiou, D. R. Roundhill, and J. E. Powers, "A new imaging technique based on the nonlinear properties of tissues," in *Proc. IEEE Ultrason. Symp.*, vol. 2, 1997, pp. 1561–1566.

[41] M. O'Donnell, "Coded excitation system for improving the penetration of real-time phased-array imaging systems," *IEEE Trans. Ultrason., Ferroelect., Freq. Contr.*, vol. 39, no. 3, pp. 341–351, May 1992.

[42] J.-y. Lu and J. Wang, "Square-wave aperture weightings for reception beam forming in high frame rate imaging," in *Proc. IEEE Ultrason. Symp.*, 2006, to be published.

[43] J. G. Abbott, "Rationale and derivation of MI and TI—A review," *Ultrasound Med. Biol.*, vol. 25, no. 3, pp. 431–441, 1999.

[44] W. D. O'Brien, Jr., Y. Yang, and D. G. Simpson, "Evaluation of unscanned-mode soft-tissue thermal index for rectangular sources and proposed new indices," *Ultrasound Med. Biol.*, vol. 30, no. 7, pp. 965–972, 2004.

[45] *AIUM/NEMA (American Institute of Ultrasound in Medicine and National Electrical Manufacturers Association). ODS. Standard for the real-time display of thermal and mechanical acoustic output indices on diagnostic ultrasound equipment, Rev 1*, Laurel, MD, and Rosslyn, VA: AIUM/NEMA, 1998.

[46] C. B. Burckhardt, H. Hoffmann, and P. A. Grandchamp, "Ultrasound Axicon: A device for focusing over a large depth," *J. Acoust. Soc. Amer.*, vol. 54, pp. 1628–1630, Dec. 1973.

[47] F. S. Foster, M. S. Patterson, M. Arditi, and J. W. Hunt, "The conical scanner: A two transducer ultrasound scatter imaging technique," *Ultrason. Imag.*, vol. 3, pp. 62–82, Apr. 1981.

[48] P. M. Morse and H. Feshbach, *Methods of Theoretical Physics, Part I.* New York: McGraw-Hill, 1953, p. 620.

[49] C. S. Kino, *Acoustic Waves: Devices, Imaging and Analog Signal Processing.* Englewood Cliffs, NJ: Prentice-Hall, 1987.

[50] R. Bracewell, *The Fourier Transform and its Applications.* New York: McGraw-Hill, 1965, ch. 4 and 6.

[51] A. C. Kak and M. Slaney, *Principle of Computerized Tomographic Imaging.* New York: IEEE Press, 1987, ch. 6.

[52] M. Born and E. Wolf, *Principles of Optics.* 7th ed. Cambridge: Cambridge University Press, 1999, ch. 13.

[53] G. C. Sherman, "Application of the convolution theorem to Rayleigh's integral formulas," *J. Opt. Soc. Amer.*, vol. 57, pp. 546–547, Apr. 1967.

[54] J. W. Goodman, *Introduction to Fourier Optics.* New York: McGraw-Hill, 1968, ch. 2–4.

[55] J. W. Cooley and J. W. Tukey, "An algorithm for the machine calculation of complex Fourier series," *Math. Comput.*, vol. 19, pp. 297–301, 1965.

[56] R. M. Lemor, P. K. Weber, P. K. Fonfara, C. Guenther, H. J. Welsch, M. L. Hoss, L. Masotti, E. Biagi, M. Scabia, A. Acquafresca, R. Facchini, S. Mazzanti, and A. Ricci, "A new combined open research platform for ultrasound radio frequency signal," in *Proc. IEEE Ultrason. Symp.*, vol. 1, 2003, pp. 33–37.

[57] P. K. Weber, H. Fonfara, H. J. Welsch, D. Schmitt, and C. Günther, "A phased array system for the acquisition of ultrasonic RF-data up to 20 MHz," *Acoust. Imaging*, vol. 27, pp. 25–32, 2003.

[58] J. A. Jensen, O. Holm, L. J. Jensen, H. Bendsen, S. I. Nikolov, B. G. Tomov, P. Munk, M. Hansen, K. Salomonsen, J. Hansen, K. Gormsen, H. M. Pedersen, and K. L. Gammelmark, "Ultrasound research scanner for real-time synthetic aperture data acquisition," *IEEE Trans. Ultrason., Ferroelect., Freq. Contr.*, vol. 52, no. 5, pp. 881–891, May 2005.

[59] M. Fink, L. Sandrin, M. Tanter, S. Catheline, S. Chaffai, J. Bercoff, and J.-L. Gennission, "Ultra high speed imaging of elasticity," in *Proc. IEEE Ultrason. Symp.*, vol. 2, 2002, pp. 1811–1820.

[60] J. C. Lacefield and R. C. Waag, "Time-shift estimation and focusing through distributed aberration using multirow arrays," *IEEE Trans. Ultrason., Ferroelect., Freq. Contr.*, vol. 48, no. 6, pp. 1606–1624, Nov. 2001.

[61] J. Wang and J.-y. Lu, "A study of motion artifacts of Fourier-based image construction," in *Proc. IEEE Ultrason. Symp.*, vol. 2, 2005, pp. 1439–1442.

[62] J. Wang and J.-y. Lu, "Motion artifacts of extended high frame rate imaging," *IEEE Trans. Ultrason., Ferroelect., Freq. Contr.*, submitted for publication.

[63] J. Wang and J.-y. Lu, "Effects of phase aberration and noise on extended high frame rate imaging," *Ultrasound Med. Biol.*, submitted for publication.
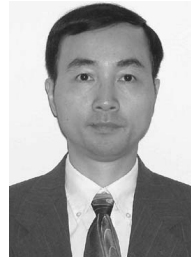
Jian-yu Lu (S'86–M'88–SM'99) received the B.S. degree in electrical engineering in February 1982 from Fudan University, Shanghai, China; the M.S. degree in acoustics in 1985 from Tongji University, Shanghai, China; and the Ph.D. degree in biomedical engineering in 1988 from Southeast University, Nanjing, China.

From 1997 to the present, Dr. Lu has been a professor in the Department of Bioengineering at the University of Toledo, Toledo, OH, and an adjunct professor of medicine at the Medical University of Ohio, Toledo, OH. He served as a graduate director of the Department of Bioengineering at the University of Toledo from 1999–2002. Before joining the University of Toledo, he was an associate professor of biophysics at the Mayo Medical School and an associate consultant at the Department of Physiology and Biophysics, Mayo Clinic/Foundation, Rochester, MN. His research interests are in acoustic imaging and tissue identification, medical ultrasonic transducers, and ultrasonic beam forming and propagation.

Dr. Lu received the Outstanding Paper Award from the UFFC society for two of his papers published in the IEEE Transactions on Ultrasonics, Ferroelectrics, and Frequency Control (UFFC) in 1992 for the discovery of X waves that, in theory, can propagate to an infinite distance without spreading (diffraction-free). These waves have potential applications in medical imaging (in both ultrasound and optics). Dr. Lu received the Edward C. Kendall (a Nobel Laureate at Mayo Clinic) Award from the Mayo Alumni Association, Mayo Foundation, in 1992, for his meritorious research; the FIRST Award from the National Institutes of Health (NIH) in 1991; and the Biomedical Engineering Research Grant Award from the Whitaker Foundation in 1991, in addition to other long-term R01-type NIH grant awards.

Dr. Lu has been the Editor-in-Chief of the IEEE Transactions on Ultrasonics, Ferroelectrics, and Frequency Control since January 2002. He is a general co-chair of the 2008 IEEE International Ultrasonics Symposium (IEEE IUS) that will be held in Beijing, China. In addition, he served as the Technical Program Chair of the 2001 IEEE IUS—a joint meeting with the World Congress on Ultrasonics (WCU) held in Atlanta, GA, in October 2001. He is a member of Group I (Medical Ultrasonics) of the Technical Program Committee of the IEEE IUS (since 2000). He also serves on both the UFFC Ultrasonics Committee and the UFFC Web Committee. He was an exhibition chair of the IEEE IUS for many years. Dr. Lu is a Fellow of the American Institute of Ultrasound in Medicine (AIUM) and a senior member of the IEEE UFFC Society, in addition to being a member of other professional societies such as the Acoustical Society of America (ASA), American Association for the Advancement of Science (AAAS), and Sigma Xi.
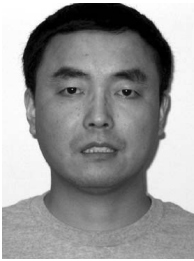
Jiqi Cheng was born in Jiangsu, China, in 1975. He received the B.S. and M.S. degrees in biomedical engineering in 1998 and 2000, respectively, both from Southeast University, Nanjing, China. He is currently pursuing his doctorate degree in the Department of Bioengineering at the University of Toledo, OH.

His research interests in ultrasound include field calculation, beam forming, transducer modeling, image formation, and medical imaging.

Jing Wang was born in Beijing, China, in 1973. He received the B.S. degree in analytical instrument engineering and the M.S. degree in precision instrument engineering in 1996 and 2000, respectively, both from Tianjin University, Tianjin, China. He is currently pursuing his doctorate degree in the Department of Bioengineering at the University of Toledo, OH.

His research interests in ultrasound include new imaging technique development and implementation, imaging process optimization, motion artifacts, and phase aberration corrections.